

# The large-scale interaction between short GRB jets and disk outflows from NSNS and BHNS mergers

GERARDO URRUTIA <sup>1</sup>, AGNIESZKA JANIUK <sup>1</sup>, FATEMEH HOSSEIN NOURI <sup>1</sup> AND BESTIN JAMES <sup>1</sup>

<sup>1</sup>*Center for Theoretical Physics, Polish Academy of Sciences, Al. Lotnikow 32/46, 02-668 Warsaw, Poland*

## ABSTRACT

Short Gamma-Ray Bursts (GRBs) are often associated with NSNS or BHNS mergers. The discovery of GW/GRB 170817A has enhanced our understanding, revealing that the interaction between relativistic jets and post-merger outflows influences the observed radiation. However, the nature of compact binary merger event suggests that the system can be more complex than the uniform jet interacting with a homologously expanding wind. We consider here an improved scenario by performing a set of two-dimensional, large scale numerical simulations, and we investigate the interaction between short GRB jets and post-merger disk wind outflows. We focus on two types of configurations, arising from NSNS and BHNS mergers. The simulations consider the effects of the r-process nucleosynthesis in the accretion disk wind on its pressure profile. The main properties of the jet, such as its energy distribution and collimation degree, are estimated from our simulations. We found that a) the impact of the r-process on initial wind pressure leads to significant changes in the jet collimation and cocoon expansion; b) the angular structure of thermal and kinetic energy components in the jets, cocoons, and winds differ with respect to simple homologous models, hence it would affect the predictions of GRB afterglow emission; c) the temporal evolution of the structure reveals conversion of thermal to kinetic energy being different for each component in the system (jet, cocoon, and wind); d) post-merger environments influence energy structure and material dispersion, altering the interaction between jets and disk winds.

*Keywords:* Accretion (14) — Gamma Ray Bursts (679) — Jets (870) — Relativistic jets (1390)

## 1. INTRODUCTION

Short gamma-ray bursts (SGRBs) are intense flashes of gamma-rays lasting  $t \lesssim 2$  s followed by a broad-band, long-lasting, afterglow radiation. These events presumably originate from binary neutron star, or black hole - neutron star mergers, as postulated by Eichler et al. (1989) and Paczynski (1991). Other scenarios, including magnetars, or accretion induced neutron star collapse, were also proposed by Berger (2011), but they do not change drastically the main picture. Once the central engine is created (a Kerr black hole surrounded by an accretion disk), the rotational energy of the black hole is transformed to the jet power, and its bulk kinetic energy, through the electromagnetic coupling (Blandford & Znajek 1977). Alternatively, annihilation of neutrino-antineutrino pairs emitted from the accretion disk may

be a source of power to the GRB jets (Popham et al. 1999; Liu et al. 2015). The emission of SGRBs is further affected by the propagation of powerful (up to  $E \sim 10^{52}$  erg) relativistic jets into a post neutron star merger environment.

From compact binary NSNS or BHNS mergers, a second electromagnetic counterpart, namely the kilonova, becomes observable. It is powered by nucleosynthesis occurring within the neutron-rich outflows after the merger (Metzger & Berger 2012). The most prominent example is the detection of GW 170817 (Abbott et al. 2017), which not only provided detailed observations of electromagnetic counterparts but also presented significant challenges for modeling. For instance, the unusual rise observed in the afterglow light curves of the *off-axis* GRB, emphasized the necessity for meticulous treatment of this component in modelling (e.g., Lazzati et al. 2018; Mooley et al. 2018).

The structure of the jet (energy and velocity distribution) plays an important role in understanding the atypical behaviour of the light curves (e.g., Granot et al.

Corresponding author: Gerardo Urrutia  
gurrutia@cft.edu.pl

2018; Lazzati et al. 2018; Mooley et al. 2018; Beniamini et al. 2020; Gill et al. 2019; Salafia & Ghirlanda 2022). After its launching, the jet acquired its structure at early times  $t \lesssim 0.1$  s due to the influence of the central engine<sup>1</sup> properties such as the black hole spin, the magnetic field strength, and the strong disk winds evolution (e.g., Aloy et al. 2005; Kathirgamaraju et al. 2019; James et al. 2022; Janiuk & James 2022). As long as the jet is evolving into a post-merger environment, the dynamics of the jet is influenced by ongoing interactions with this environment. In consequence, its structure can be modified far from the central engine (e.g., Lazzati et al. 2018; Lazzati et al. 2021; Hamidani et al. 2020; Murguia-Berthier et al. 2021).

The interaction of the jet with the post-merger environment has been intensively studied with numerical simulations. This environment has been mainly described in two approaches. The first is to assume as a spherical wind expanding homologously and parametrized by its mass loss rate  $\dot{M}_{\text{wind}}$  and velocity (Murguia-Berthier et al. 2014; Hamidani et al. 2020; Urrutia et al. 2021; Nativi et al. 2022; Hamidani & Ioka 2023; Mpisketzis et al. 2024). Alternatively, the wind can also be described by homologous toroidal winds, whose angular profiles of density  $\rho_{\text{wind}}(r, \theta)$  and velocity  $v_{\text{wind}}(r, \theta)$  were extracted from neutrino driven or strongly magnetized winds (Aloy et al. 2005; Murguia-Berthier et al. 2017; Nativi et al. 2020; Murguia-Berthier et al. 2021). In addition to the wind characteristics, the dynamics of weakly magnetized jets has been explored (Nathanail et al. 2020; Gottlieb & Nakar 2021) and the impact of the magnetized environment (e.g., García-García et al. 2023). In all these works, a wide range of the wind properties and jet such as the luminosity  $L_j$ , Lorentz factor  $\Gamma_j$ , and launching time  $t_j$  were explored. In consequence, it was shown that the jet structure and its dynamics is modified.

The second approach to study the jet-wind interaction, is to import the post-merger environment from simulations that evolve the binary NSNS coalescence until the creation of hypermassive neutron star (HMNS) (e.g., Ciolfi et al. 2017; Ciolfi et al. 2019). The results are remapped in a new numerical setup and the hydrodynamical evolution of the jet is analyzed (e.g., Lazzati et al. 2021; Pavan et al. 2021). The post-merger environment is not only described by density and velocity distri-

butions. In addition, it presents turbulence and geometrical evolution of magnetic fields (Combi & Siegel 2023; Pavan et al. 2023). However, in these works, the collapse of HMNS to a black hole was followed analytically, and the accretion disk formation was not considered. On the other hand, the evolution of accretion disk and jet from small to large scales has been solved, respectively, for NSNS and BHNS merger by Gottlieb et al. (2022, 2023), showing that this component impacts the large-scale evolution of the jet. In conclusion, each component of the post-merger environment (the post-merger ejecta and the accretion disk wind) modifies the dynamics of the jet.

The postmerger accretion disk's characteristics depend on the compact object merger parameters such as mass ratio, neutron star's equation of state and BH spin (in the case of BHNS) (Lovelace et al. 2013; Foucart et al. 2013; Krüger & Foucart 2020). Magnetic field and neutrino particles are the main rulers of the postmerger disk evolution. In addition to launching jets, magnetic field is responsible for heating the plasma (Sano et al. 2004; Hossein Nouri et al. 2018) and emergence of the magnetically-driven winds (Fernández et al. 2019; Janiuk 2019; Fahlman & Fernández 2022). They transport the angular momentum outwards, due to magnetorotational instability (MRI) (Balbus & Hawley 2002). On the other hand, since the postmerger disks are optically thin for neutrinos, the thermal energy can be lost by neutrino radiations. Moreover, neutrinos provide mechanisms for neutrino viscosity (Guilet et al. 2015, 2017) and launching thermal winds through neutrino absorption (Perego et al. 2014; Martin et al. 2015). Therefore, both magnetic field and neutrinos have contributions in the thermal evolution and launching neutron-rich outflows for the r-process nucleosynthesis. The r-process is believed to be the origin of kilonova emissions and creation of the heavy elements in the Universe (Woosley & Hoffman 1992; Kasen et al. 2017; Tanaka et al. 2017). It is important to note that the outflows properties (such as velocity, composition, temperature and opacity) are not only affected by the launching mechanism in the accretion disk, but also continuously change as a result of the heat released by the r-process nucleosynthesis in a timescale of  $\sim 1$  s, hence in a realistic scenario, the ejecta's properties are more complex than a simple homologously expanding wind.

In this work, we study how the outflow from the post-merger disk impacts the propagation of the jet. In particular, we focus on two main progenitor types: the outflows originating from the central engines formed after the NSNS and BHNS mergers. The accretion disk wind profiles were obtained from numerical general relativistic

<sup>1</sup> The structure of the jet shaped at small scales can be partially preserved at large scales if the interaction is with a low-density environment, for example  $\dot{M} \sim 10^{-4} M_{\odot} \text{ s}^{-1}$  (Urrutia et al. 2021) and lost for denser environments  $\dot{M} \sim 10^{-2} M_{\odot} \text{ s}^{-1}$  (Nativi et al. 2022; Urrutia et al. 2022).

tic (GR MHD) simulations in Kerr metric, and then remapped onto a new setup to follow the large-scale jet evolution at late times. In our analysis, we distinguish each component of the post-merger environment to emphasise the influence of the disk wind outflow on the jet properties. We also highlight the differences in comparison to the impact of a homogenous post-merger environment.

This paper is structured as follows: In Section 2 we describe our physical assumptions, the numerical setup, and how the disk wind is collected. In Section 3 we present our results, and Section 4 is dedicated to discussing the contribution of the disk wind regarding a homogeneous environment. Finally, in Section 5 we summarize our results.

## 2. METHODS

### 2.1. Numerical Setup

We perform two-dimensional simulations of Special Relativistic Hydrodynamics (SRHD) to study the interaction between short GRB jets and the post-merger disk wind. We use the Adaptive Mesh Refinement (AMR) *Mezcal* code (De Colle et al. 2012), which employs a second-order solver for both space and time to solve the SRHD equations. Primitive variables density  $\rho$ , velocities  $v_j$ , and pressure  $p$  are determined through the evolution of conservative variables  $D = \Gamma\rho$ ,  $m_j = Dh\Gamma v_j$ , and  $\tau = Dh\Gamma c^2 - p - Dc^2$ , by solving the system of equations

$$\frac{\partial \mathbf{U}(\mathbf{w})}{\partial t} + \frac{\partial \mathbf{F}^i(\mathbf{w})}{\partial x^i} = 0. \quad (1)$$

Here, the conservative components are  $\mathbf{U}(\mathbf{w}) = (D, m_j, \tau)$ , the flux is  $\mathbf{F}^i(\mathbf{w}) = (Dv^i, m_j v^i + p\delta_j^i, \tau v^i + p v^i)$ , and  $\Gamma$  represents the Lorentz factor. For the flux calculation, the Harten, Lax and van Leer Contact (HLLC) Riemman Solver (Mignone & Bodo 2005) is employed, which is a less dissipative method that allows following turbulence. Additional details about the *Mezcal* code can be found in De Colle et al. (2012).

We follow the jet and wind propagation during 4 seconds of integration time. The initial conditions are imposed through the primitive variables ( $\rho, v_j, p$ ) at an inner boundary located at  $r_{\text{in}} = 3 \times 10^8$  cm. We use a two-dimensional computational box in a spherical coordinate system. It is extended radially from  $r_{\text{inj}}$  to  $1.2 \times 10^{11}$  cm, while the angular polar direction  $\theta$  covers from 0 to  $\pi$ .

For the grid configuration, we employ a number of cells  $N_r = 1 \times 10^4$  along  $r$  direction, and  $N_\theta = 100$  in  $\theta$  direction. We use  $n_l = 4$  levels of refinement which, under our configuration, being  $r_{\text{max}} = 1.2 \times 10^{10}$  cm,  $r_{\text{min}} =$

$3 \times 10^8$  cm and  $\theta_{\text{max}} = \pi/2$ , the maximum resolution at the smallest cells is  $\Delta r = (r_{\text{max}} - r_{\text{min}})/(N_r \cdot 2^{n_l-1}) \approx 1.49 \times 10^6$  cm and  $r_{\text{min}}\Delta\theta = r_{\text{min}}\theta_{\text{max}}/(N_\theta \cdot 2^{n_l-1}) \approx 1.17 \times 10^6$  cm.

### 2.2. Physical scenario and assumptions

We filled the computational box with a low-density medium  $\rho_a = 10^{-5}$  g/cm $^{-3}$  to avoid numerical errors during the evolution of our short GRB models.

The short GRB scenario<sup>2</sup> considered for this work consists of the combination of three elements, assuming that binary NSNS or BHNS merger has been done. 1) The post-merger ejecta (PME) expelled after the merger  $t > t_{\text{merger}}$ , 2) the post-merger disk wind outflow (OUT) formed after  $t > t_{\text{collapse}}$  and 3) the relativistic jet which is launched during the collapse as well (see Fig. 1). The binary BHNS scenario does not experience a collapse, resulting in a distinct structure of the PME compared to the NSNS case. However, for simplicity, we adopt a similar expanding PME approach until  $t_{\text{collapse}} \sim 0.1$  s. This study primarily focuses on the evolution of short GRB models beyond  $t_{\text{collapse}}$ , based on components 2) and 3).

In our study, we perform a case control without PME to investigate only the propagation of jets and winds. These elements propagate in the constant density medium  $\rho_a$  neglecting any environmental effects caused by PME. This case is denoted as ‘‘NO’’ in Table 1.

To consider the effect of PME, we launch a spherical ejection during  $t \lesssim 0.1$  s, i.e., before the launching of the disk-wind and jet. The density of PME is given by

$$\rho_{\text{ej}} = \frac{\dot{M}}{4\pi r_{\text{inj}}^2 v_{\text{ej}}}, \quad (2)$$

and a velocity of  $v_{\text{ej}} = 0.1c$ . We assume that this PME has a mass loss rate of  $\dot{M} = 10^{-2} M_\odot \text{ s}^{-1}$  (e.g., Combi & Siegel 2023). It is designated as ‘‘EJ’’ in Table 1.

A second case of PME is assumed as a spherical atmosphere (e.g., Lazzati et al. 2021) described by

$$\rho_f(r) = \rho_* e^{-r/r_{\text{inj}}}, \quad (3)$$

where we fixed  $\rho_* = 10^{-2} M_\odot \text{ s}^{-1} / (4\pi r_{\text{inj}}^2 \cdot 10^{-1}c)$ . The objective of this scenario is to study the propagation of jets in an environment while mitigating the impact of disk wind effects. In Table 1, this case is denoted as ‘‘SPH’’.

In our study, we employ a simplified description of PME. Our main interest is to study the properties of

<sup>2</sup> A complete picture of Short GRB evolution (including the effects of tidal tail) is discussed, for example, in Murguia-Berthier et al. (2017).

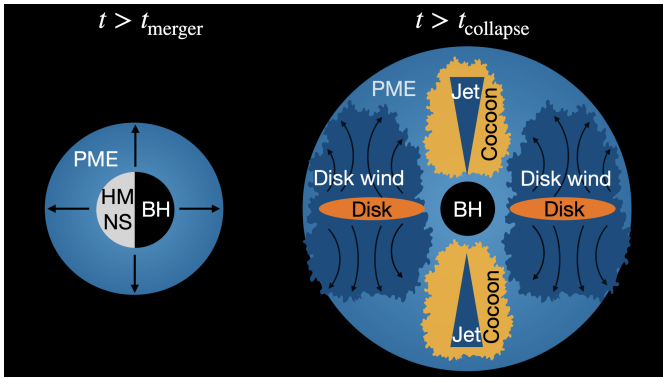


**Figure 1.** A non scaled cartoon of a post binary NSNS (or BHNS) merger. At the left, we assume that the remnant material, namely PME, is expelled uniformly until the collapse of HMNS to BH. During the time of collapse, assumed  $t_{\text{collapse}} = 0.1$  s, the PME suffers an initial expansion and fills the initial environment where the jet and disk-wind will be propagating. The case of binary NSBH does not suffer a collapse, however for simplicity we assume the same expansion time for PME. This study is focused on the evolution of short GRB models for  $t > t_{\text{collapse}}$ .

the jet interaction with the post-merger disk outflow. In the following sections, we describe in detail the implementation of these elements.

### 2.2.1. Collecting a strong disk wind and the influence of $r$ -process over the gas pressure

We map a disk wind outflow as an initial condition at the inner boundary located at  $r_{\text{inj}}$ . The strong outflows were originated by the accretion of high-spinning black holes. We assume that the system, consisting of a black hole and an accretion disk, here after named the central engine, has already been formed. In particular, we collect data from configurations post binary NS-NS merger, and BH-NS merger. The evolution of the central engines was performed by Nouri et al. (2023) for a few cases of 2D magnetized accretion disks, each resembling different possible scenarios of postmerger disks from compact object collisions. We selected two cases, namely M2.65-0.1-a0.9 and M5.0-0.3-a0.9 from this study, which refer to NSNS and BHNS postmerger disks respectively. The key parameters for defining these configurations, which include the black hole’s spin, mass, and the accretion disk’s mass at the initial time, can be found in Table 1. These systems were evolved for  $t_{GR} = 2 \times 10^4$  in geometric units:  $G = c = M = 1$ , which is equivalent to  $\sim 0.35$ s for NSNS and  $\sim 0.4$ s for BHNS in the physical units according to  $t_g \equiv GM_{\text{BH}}/c^3$  unit conversion. These simulations were performed by the General Relativistic Magneto Hydrodynamic (GRMHD) HARM-COOL code (Janiuk 2019) which is the developed version of HARM (Gammie et al. 2003). In this

version, the plasma is defined with a realistic nuclear equation of state composed of free protons, neutrons, electron-positron pairs, and helium nuclei. The fraction of each species is determined by the equilibrium condition assumed for weak nuclear reactions. The neutrino cooling effect was included in this study and computed from the optical depth of each lepton-flavour neutrinos, which is approximated from neutrino’s absorption rates. The details of the microphysics treatment for these simulations are given in Janiuk et al. (2013), Janiuk (2017) and Janiuk (2019).

The evolution of the disk wind outflow is followed by copious number of tracer particles. The tracer particle technique implemented in HARM.COOL code has been described in detail in Janiuk (2019). In the initial state of the GR MHD simulation, we initialize tracers in the grid, restricted to the densest parts of the flow, i.e. in the torus body. The code follows their trajectories in time, and those which leave the outer boundary, are saved as ‘outflow tracers’. As verified by Nouri et al. (2023), the actual outflow mass computed from tracers is lower, than the estimated value from Bernoulli criterion. Nevertheless, we use the tracer information here, as it carries important quantities, such as the density, and nuclear pressure of the outflowing wind. The two panels in Fig. 2 refer to the disk wind outflows chosen from the work of Nouri et al. (2023).

We determine the composition of the ejecta through post-processing of the tracers using the SkyNet nuclear reaction network (Lippuner & Roberts 2017), which calculates the rate of change of abundance  $\dot{Y}_i$  for each individual species  $i$ , taking into account the reaction rates, velocity-averaged cross-sections, and the density history provided by the tracers. The temperature evolved in the network is influenced by  $r$ -process.

The energy released during the  $r$ -process influences the environment, for example, affecting the pressure which is a pivotal component in the simulations conducted in the new study. We considered a shorter timescale for the  $r$ -process evolution ( $t \lesssim 0.4$  s) based on the time which takes the tracers to reach the inner boundary at  $r_{\text{inj}}$  (individually, each of them touches the inner boundary at different fractions of second). At this particular point, we extract the pressure of each tracer by employing an inversion of the Helmholtz equation, employing the code presented by Timmes & Arnett (1999).

Since the integration time  $t_I$  of the large-scale SRHD simulations is greater than the integration time  $t_{GR}$  GRMHD simulations, we assume that time-averaged distributions can be approximated as  $\rho(t > t_{GR}) \propto \rho(t/t_{GR})^{-5/3}$ . Examples of snapshots of distributions are shown in Fig. 3. The outflows properties are in-

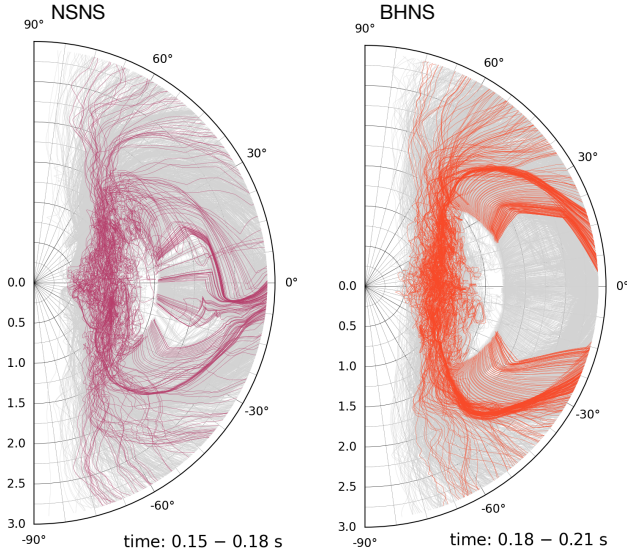


**Figure 2.** The trajectories of outflow tracers projected onto a polar map with coordinates  $(\log[r/r_g], \theta)$ . The high-opacity trajectories represent a specific range of arrival times at the external boundary of the GRMHD simulations, which is the internal boundary in SRHD simulations.

investigated in details by [Nouri et al. \(2023\)](#). Generally, there are common features shared by all the cases, for instance, the faster and less neutron-rich outflows are distributed on the poles as shown in [Fig.3](#). On the other hand, the outflows are more massive on the equator. However, there are some distinguishable features between BHNS and NSNS cases; The average electron fraction is higher for the BHNS case especially on the equator, predicting a less effective r-process nucleosynthesis for this case.

### 2.2.2. The jet implementation

For the jet implementation, we consider the total energy density

$$e_{\text{tot}} = \Gamma^2 h \rho c^2 - p - \Gamma \rho c^2, \quad (4)$$

being  $h = 1 + \frac{\gamma}{\gamma-1} p / \rho c^2$  the enthalpy. By taking the adiabatic index as  $\gamma = 4/3$  and arrange the terms, we can describe contributions by components (e.g., [Suzuki & Maeda 2022](#); [Urrutia et al. 2022](#)), respectively, the kinetic energy density

$$e_{\text{kin}} = \Gamma (\Gamma - 1) \rho c^2, \quad (5)$$

and, the thermal energy density

$$e_{\text{th}} = p (4\Gamma^2 - 1). \quad (6)$$

The jet is imposed within an angular region of  $\theta_j = 15^\circ$ , determined by the mass distribution of the wind

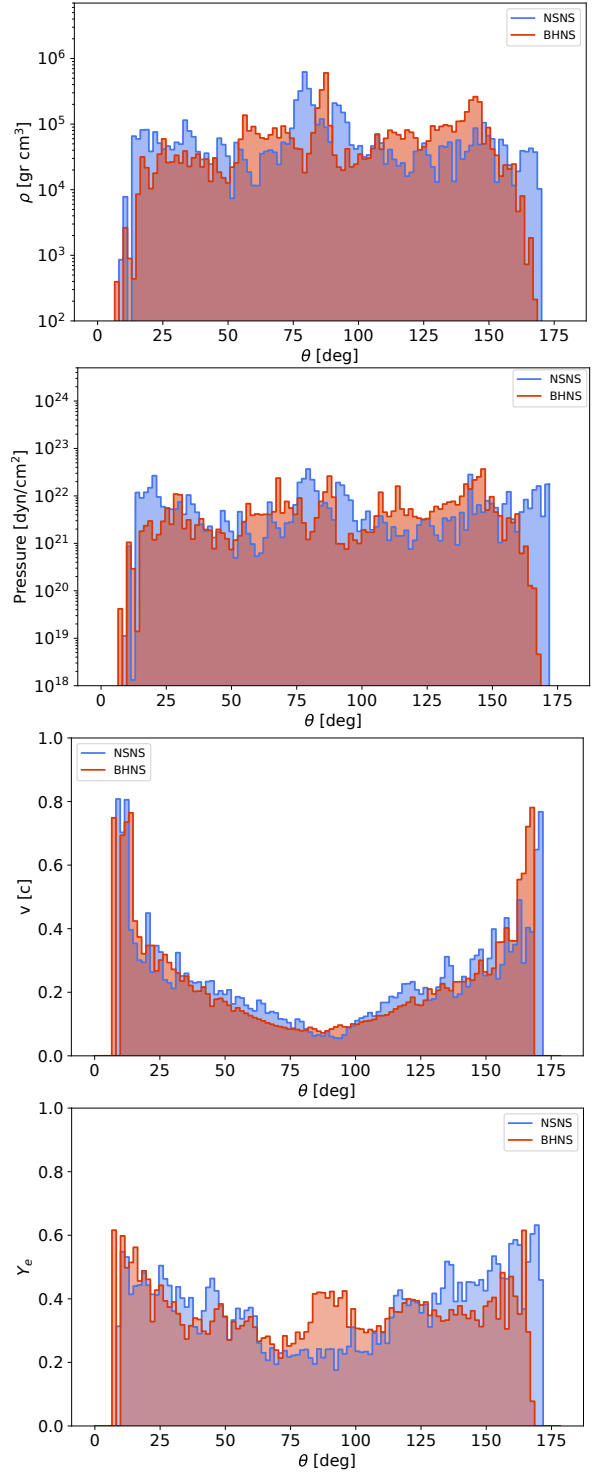


**Figure 3.** Snapshot at  $t = 0.3$  s of the outflow distribution. This data was obtained by collecting and averaging information from tracer particles that reached the injection radius  $r_{\text{inj}}$ . The values for pressure and electron fraction  $Y_e$  were determined through the r-process.

(Fig. 3), specifically excluding the regions near the poles where the wind coverage is absent. Within these regions, we estimate the jet luminosity, by applying the surface integral (energy flux) of both contributions (kinetic and thermal) in (4), i.e.,

$$L_j = 2\pi \int_0^{\theta_j} e_{\text{tot}} v_r r_{\text{inj}}^2 d\theta. \quad (7)$$

The surface integral was estimated based on the final snapshot obtained with GRMHD simulation, but, vanishing the magnetic contribution, since our large-scale simulations are hydrodynamical<sup>3</sup>. The extracted values of luminosity are resumed in Table 1. We assumed a jet dominated by pressure<sup>4</sup>  $e_{\text{th}} \gg e_{\text{kin}}$  (e.g., Urrutia et al. 2022), and a continuous jet injection with a terminal Lorentz factor given by

$$\Gamma_\infty = h_j \Gamma_j, \quad (8)$$

being the enthalpy of the jet  $h_j = 1 + 4p_j/\rho_j c^2$ . Here after, sub index  $j$  denotes physical quantities associated to the jet. Since the jet is already dominated by thermal pressure ( $h_j \gg 1$ ), we assume a fixed value of terminal Lorentz factor of  $\Gamma_\infty = 100$  to regulate the pressure of the jet  $p_j$  during its continuous injection. Taking  $\Gamma_{\text{ad}} = 4/3$ , by the substitution of enthalpy  $h_j = 1 + 4p_j/\rho_j c^2$ , the pressure of the jet can be written as

$$p_j = \frac{\rho_j c^2}{4} \left( \frac{\Gamma_\infty}{\Gamma_j} - 1 \right). \quad (9)$$

The density of the jet is obtained by the mixing of equations (4) and (7)

$$\rho_j = \frac{L_j}{\Gamma_\infty \Gamma_j v_j c^2 \Delta S}. \quad (10)$$

For a spherical head of the jet,  $\Delta S = 4\pi(1 - \cos \theta_j) r_j^2$ . The injection time for the jet  $t_j$  is restricted by the averaged mean time life of the central engine (Kluźniak & Lee 1998; Lee & Ramirez-Ruiz 2002; Janiuk & Proga 2008), approximated by  $t_j = m_d / \langle \dot{M}_{\text{out}} \rangle$ . For this work, we use the values described in Table 1 which are consistent in the time ranges of short GRBs.

### 2.3. The energy extraction for post-processing analysis

We define the total energy contribution as the sum of the energy enclosed in all cells (e.g., Urrutia et al. 2021, 2022; Nativi et al. 2022)

$$E = \int e_{\text{tot}} dV. \quad (11)$$

<sup>3</sup> More complete calculation of the energy extraction including the Poynting energy contribution is provided in James et al. (2022); Janiuk & James (2022).

<sup>4</sup> Discussion of jet launching schemes e.g. Urrutia et al. (2022).

The contribution of independent components, kinetic or thermal, respectively in eqs. (5) and (6), (e.g., Suzuki & Maeda 2022) by the integration of  $e_{\text{kin}}$  or  $e_{\text{th}}$ , instead of  $e_{\text{tot}}$ . We divide the contributions of each component of the relativistic and sub-relativistic material, by a selection of how fast it moves. The jet is defined as the faster material,

$$E_{\text{jet}} \equiv E(\Gamma \geq \Gamma_j), \quad (12)$$

and the cocoon as a intermediate values

$$E_{\text{cocoon}} \equiv E(2 \leq \Gamma < \Gamma_j). \quad (13)$$

The contribution of the wind requires and spacial treatment since the velocities are sub-relativistic. Following the definition of total energy in eq. (4), the Lorentz factor in the kinetic contribution eq. (5), i.e., has influence  $f(\Gamma) \equiv \Gamma(\Gamma - 1)$ . For a smoothed transition close to  $\Gamma \sim 1$ , we fix a minimum value  $\Gamma_{\text{min}} = 1.1$  that corresponds to a minimum wind velocities of  $\beta \sim 0.1c$  and we took the Taylor expansion of  $f(\Gamma)$  close to  $\Gamma_{\text{min}}$ . The kinetic contribution of the wind is expressed as

$$e_{\text{w,kin}} = \frac{1}{2} D \beta^2 c^2, \quad (14)$$

where the rest mass in this limit is  $D \equiv f(\Gamma) \rho$ . The thermal energy remains unaffected close to  $\Gamma_{\text{min}}$  because the vales  $e_{\text{th}} \sim 3p$ . The energy of the wind is selected trough a threshold of velocities

$$E_{\text{wind}} \equiv E(0.1 \leq \beta < 0.4) \quad (15)$$

which represents the contribution of the mos slower material in the system. A similar selection with 4-velocity is made by Suzuki & Maeda (2022) and trough the asymptotic Lorentz factor by Lazzati et al. (2021); García-García et al. (2023).

## 3. RESULTS

In this Section we present the results of our calculations. First, we describe interaction of jet with post-merger wind from accretion disk. Second, we discuss two additional test models which present jet interaction with spherical wind, from a hyper massive neutron star launched before its collapse. Third, we present evolution of jet and cocoon and their energy.

### 3.1. Jet and wind interaction

In Fig. 4 we present colour maps showing the jet and wind structure, taken at a time  $t = 0.4$  s for the models considered in this study. The columns display specific models categorized into two groups describing the scenarios of jet interaction with outflows resulting from

Model	$L_j$ [erg s $^{-1}$ ]	$\theta_j$ [deg]	$\Gamma_j$	$t_j \sim t_{CE}$	$M_{BH}$	$a$	$M_{disk}$	$M_{out}$ [ $M_\odot$ ]	$\dot{M}_{out}$ [ $M_\odot$ s $^{-1}$ ]	PME
NSNS1	$1.4 \times 10^{50}$	15°	7.4	1.57	2.65	0.9	0.10276	$7.691 \times 10^{-4}$	$3.27 \times 10^{-2}$	NO
NSNS2	$1.4 \times 10^{50}$	15°	7.4	1.57	2.65	0.9	0.10276	$7.691 \times 10^{-4}$	$3.27 \times 10^{-2}$	EJ
SPH1	$1.4 \times 10^{50}$	15°	7.4	1.57	–	–	–	No disk wind	–	SPH
SPH2	$1.4 \times 10^{50}$	8°	7.4	1.57	–	–	–	No disk wind	–	SPH
BHNS1	$2.13 \times 10^{50}$	15°	12	1.07	5	0.9	0.3120	$6.558 \times 10^{-3}$	$1.49 \times 10^{-1}$	NO
BHNS2	$2.13 \times 10^{50}$	15°	12	1.07	5	0.9	0.3120	$6.558 \times 10^{-3}$	$1.49 \times 10^{-1}$	EJ
SPH3	$2.13 \times 10^{50}$	15°	12	1.07	–	–	–	No disk wind	–	SPH
SPH4	$2.13 \times 10^{50}$	4.7°	12	1.07	–	–	–	No disk wind	–	SPH

**Table 1.** The list of the models performed in our study, detailing their main parameters and scenarios. The left panel contains the jet parameters extracted from the GRMHD simulation data performed by Nouri et al. (2023), whereas the right panel presents the configuration of the central engine. This table is divided into two sections: the upper section defines the post-binary NSNS merger scenario, and the lower section corresponds to the post-binary BHNS merger scenario.

either binary NSNS or BHNS mergers. The numerical labels, ‘1’ or ‘2’, indicate whether the jet and outflow are interacting with an initial PME. Each row corresponds to a physical quantity: thermal energy  $e_{th}$ , enthalpy  $h - 1 = 4p/(\rho c^2)$ , module of four-velocity  $u = \Gamma\beta$  and density  $\rho$ , respectively. Details of each model are summarized on the Table 1.

The global morphology of our models is a consequence of the interaction between the jet and wind at early times (e.g.,  $t \sim 0.4$  s). During this early phase, turbulence plays an important role in mediating the interaction dynamics. This interaction can be observed in the results of the NSNS2 and BHNS2 models, where both the jet and wind suffer a smooth breakout from the initial ejecta at  $t \sim 0.1$  s. The density and pressure of the wind pushes the weak cocoon, and in consequence it collimates the jet through pressure balance. An opposite result is observed for the dynamics of NSNS1 and BHNS1. In the case of BHNS1, the limited interaction between the jet and wind results in an accelerated radial expansion. Moreover, the NSNS1 model exhibits a notable asymmetry at the southern pole due to the absence of initial ejecta able to obstructing the wind radial expansion.

The thermal energy density map (1st row) provides a qualitative visualization of the interaction between the jet and the wind. In the models NSNS1 and BHNS1, the thermal energy presents a significant concentration close to the poles and a poor concentration at the equator. The distribution of thermal energy became more uniform for the models NSNS2 and BHNS2.

The enthalpy map (2nd row) reveals regions where thermal energy dominates over the rest-mass energy. These heated regions are primarily concentrated in the zones of interaction, and they refer to the jet and cocoon balance, the cocoon-wind transition, and the shock at the boundary with the external low-density gas. In particular, this external shock creates a shell of swept-up

material, which is more pronounced for the NSNS1 and BHNS1 models.

The colour map representing the velocity (3rd row) provides a quantitative structure of the jet ( $u \sim 0.9\Gamma_j$ ), cocoon ( $0.9\Gamma_j \gtrsim u \gtrsim 2$ ), and wind ( $u \lesssim 2$ ). Darker regions correspond to material with  $\beta \leq 0.1$  since we mark this minimum in the colour map. In both NSNS1 and NSNS2 models, the wind significantly impacts the jet, leading to its collimation. The south pole of NSNS1 exhibits a whiplash effect, resulting in the creation of a faster shell. The BHNS maps illustrate the propagation of jets injected with high Lorentz factors, as detailed in Table 1. The jet channel maintains expansion in BHNS1 and remains collimated in BHNS2. Both models produce fast external shells. The wind velocity in all models maintains sub-relativistic speeds due to denser outflows.

The density maps (4th row) illustrate the asymmetrical distribution of ejected material. Notably, denser material exhibits an accumulation towards the inner regions. This behaviour can be attributed to heavy material tending to maintain lower velocities. A substantial fluid, characterized by high density concentrations, exhibits a less diffusive propagation. For example, the fluid in BHNS scenario imposed as a massive ejection (see Table 1) is more diffusive than in the NSNS scenario, which displays a high degree of mixing. In addition, regions of turbulence become apparent in regions of transition marked by abrupt changes in velocity, indicative of hydrodynamic instabilities.

### 3.2. Jet propagation in spherical wind

To evaluate the contribution of the disk wind to the propagation of sGRB jets and for a comparative analysis, we performed four additional jet models propagating within a simplified spherical atmosphere, excluding any interactions with the disk wind. For comparison with the merger scenario, we study two types of jets (detailed in Table 1): the non-collimated jet models SPH1

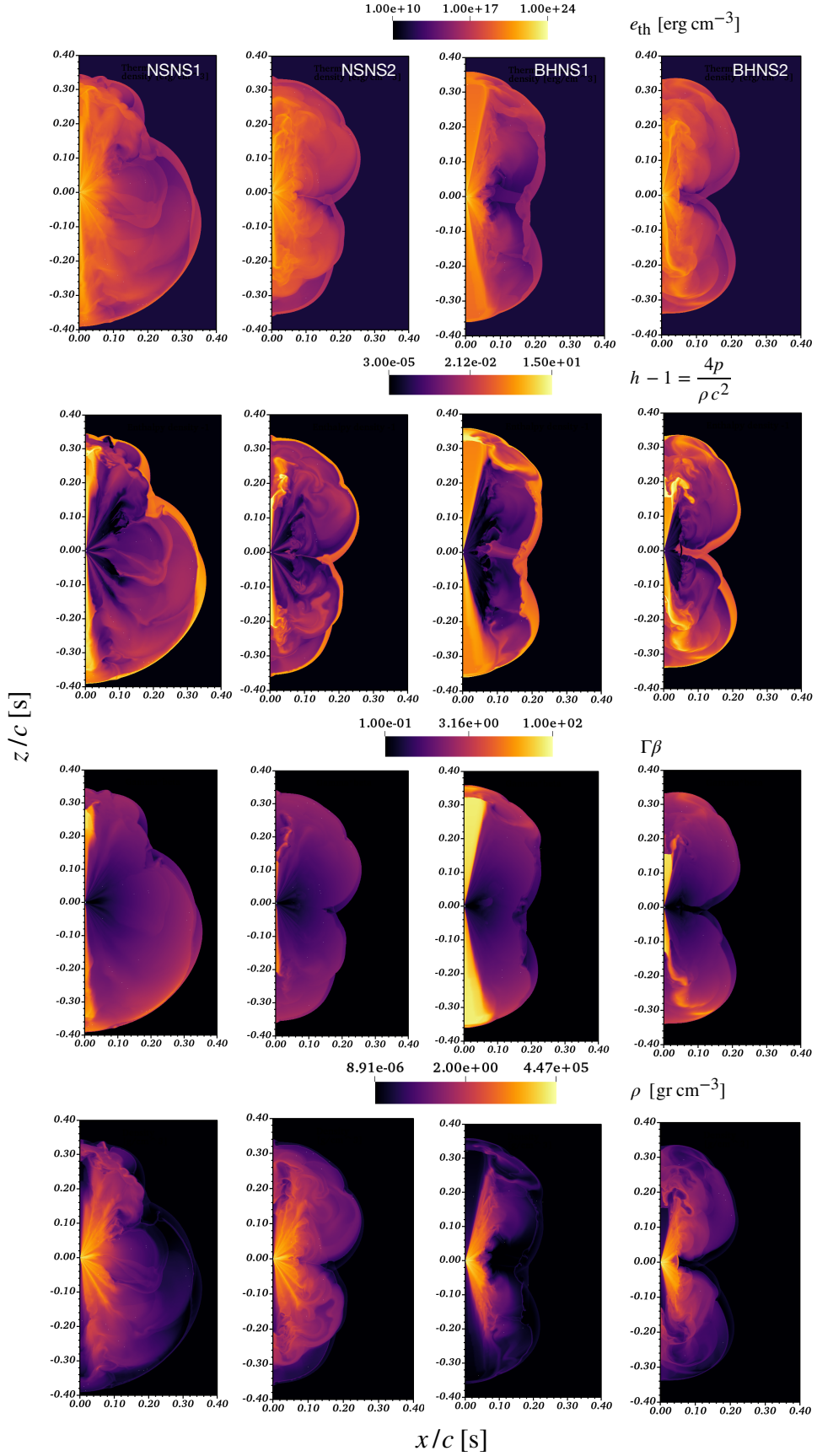


**Figure 4.** Color maps at  $t = 0.4$  s. Columns depict the models NSNS1, NSNS2, BHNS1, and BHNS2 (as detailed in Table 1). Rows showcase density maps of thermal energy  $e_{\text{th}}$ , enthalpy  $h - 1$ , four velocity  $\Gamma\beta$ , and density  $\rho$ , respectively from top to bottom. The axis are normalized by the speed of light  $c$ .



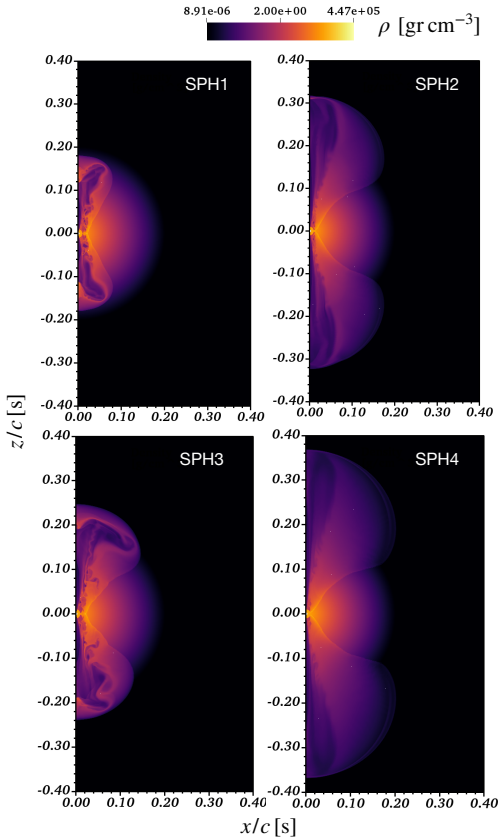


**Figure 5.** Density maps at  $t = 0.4$  s of jets propagating into a spherical atmosphere without wind contribution. In the upper panel, the models SPH1 and SPH2 belong to the group post binary NSNS merger, while in the lower panel SPH3 and SPH4 belong to the group post binary BHNS merger as we shown in Table 1.

and SPH3 where  $\theta_j < 15^\circ$ , and the collimated jet models SPH2 and SPH4, where  $\theta_j < 1/\Gamma_j$  (e.g., Bromberg et al. 2011). Fig. 5 presents the density maps, the upper panel belongs to NSNS scenario and bottom to BHNS scenario. These maps revealing a slow propagation for non collimated jets, while the collimated cases present the formation of re-collimation shocks and the expansion of the cocoon according to the decline of atmosphere density.

### 3.3. Chemical composition of the wind

Studying the chemical composition of the disk wind and its interaction with the jet and dynamical ejecta is crucial for kilonova light curves predictions. In a merger scenario, the less neutron-rich and more transparent disk wind is being surrounded with more opaque and neutron-rich dynamical ejecta produced during merger (Metzger et al. 2010; Grossman et al. 2014; Kawaguchi et al. 2016). Based on study by Kasen et al. (2015) with radiative transfer code, the presence of even a small amount of overlying, neutron-rich dynamical

ical ejecta ( $10^{-4}M_\odot$ ) will act as a ‘lanthanide-curtain’ blocking the optical wind emission from certain viewing angles. The *Mezcal* code (De Colle et al. 2012), employed in the present study, is not formulated for radiative transfer and composition evolution, therefore we limit our discussion to the qualitative geometrical evolution of the wind contains matter with different electron fractions.

To follow a qualitative evolution of different components of the disk wind outflow (Fig. 3), we tracked the distribution of the ejected material using passive scalars associated with different ranges of electron fraction as

$$(Y1, Y2, Y3, Y4) = \begin{cases} (1, 0, 0, 0) & \text{if } 0.1 < Y_e \leq 0.2, \\ (0, 1, 0, 0) & \text{if } 0.2 < Y_e \leq 0.3, \\ (0, 0, 1, 0) & \text{if } 0.3 < Y_e \leq 0.4, \\ (0, 0, 0, 1) & \text{if } 0.4 < Y_e \leq 0.5. \end{cases} \quad (16)$$

Every component  $Y_i$  represents the composition of the disk wind and evolves together with the fluid parcels. In Fig. 6 at  $t = 2$  s, we show the tracked composition, where the most contrasting regions highlight the abundance of each component.

Rich lanthanide outflows can be categorized based on the electron fraction  $Y_e \leq 0.25$  (e.g., Metzger & Berger 2012; Rosswog & Korobkin 2022). In Fig. 6, components Y1 and Y2 represent qualitatively the segments characterized by a low electron fraction (the red kilonova component with high opacity), while components Y3 and Y4 represent segments with a higher electron fraction and low opacity (blue component).

In the case of NSNS1, this material accumulates closer to the equatorial region, whereas in NSNS2, it is confined to a smaller area. In contrast, the BHNS model exhibits a notably different distribution of high-opacity material, in an intermediate region between the poles and the equator. In both scenarios, the presence or absence of post-merger ejecta (PME) strongly regulates the distribution of the components.

### 3.4. Propagation of shock front

In Fig. 7 we show the propagation of the shock front  $r_{j,sh}$  for each jet listed in Table 1. During the initial two seconds of evolution, collimated models can be distinguished because each of them produces different acceleration. However, at later times, the propagation becomes similar. On the other hand, non-collimated jets, SPH1 and SPH3, which start with different values of  $\Gamma_j$ , exhibit a remarkable difference in their propagation evolution. This discrepancy is due to their jet heads not

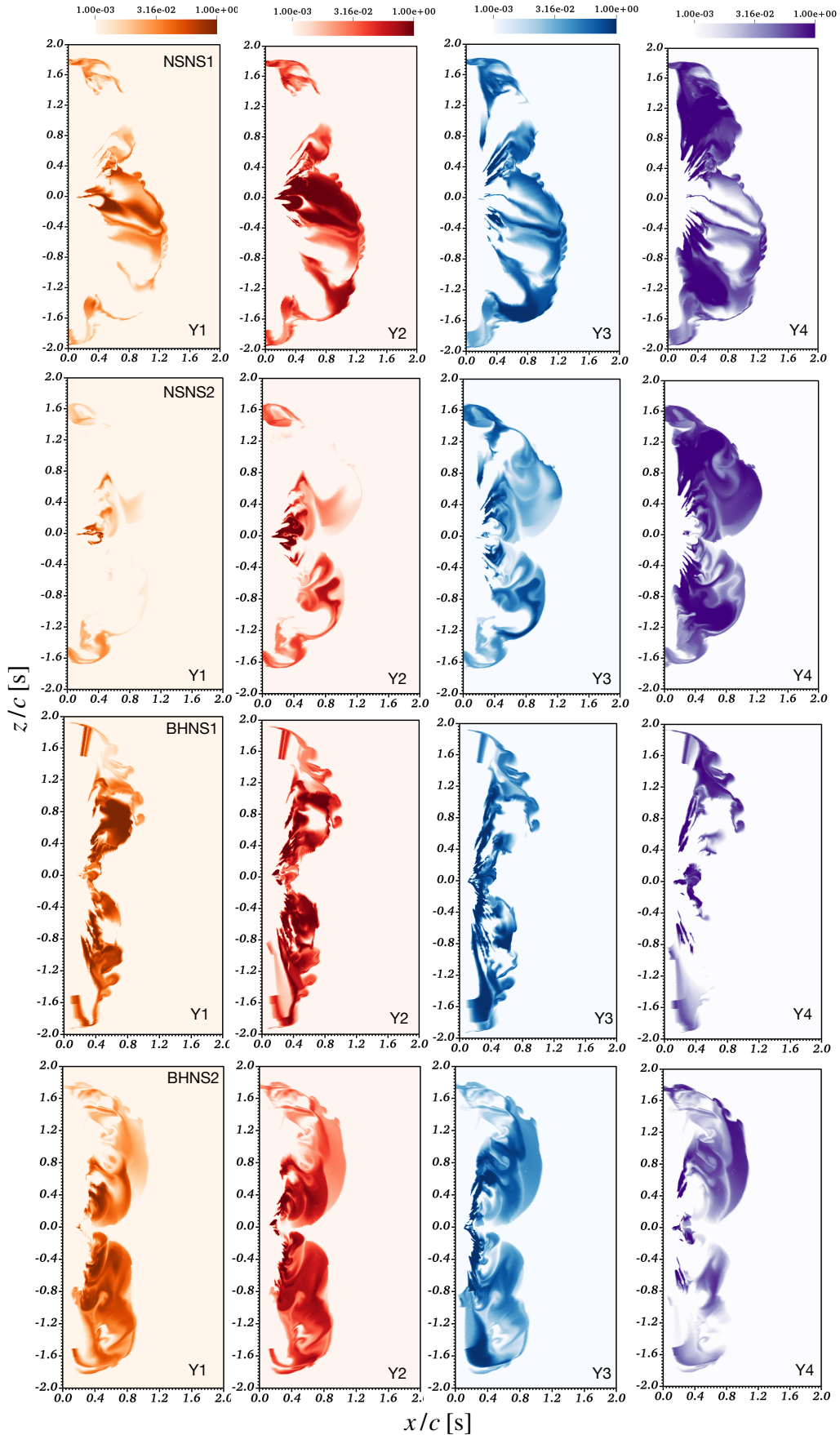


**Figure 6.** Components (Y1, Y2, Y3, Y4) of the disk wind tracked at 2 s. These components are evolved as passive scalars, related with the electron fraction  $Y_e$  as defined in Equation 16.

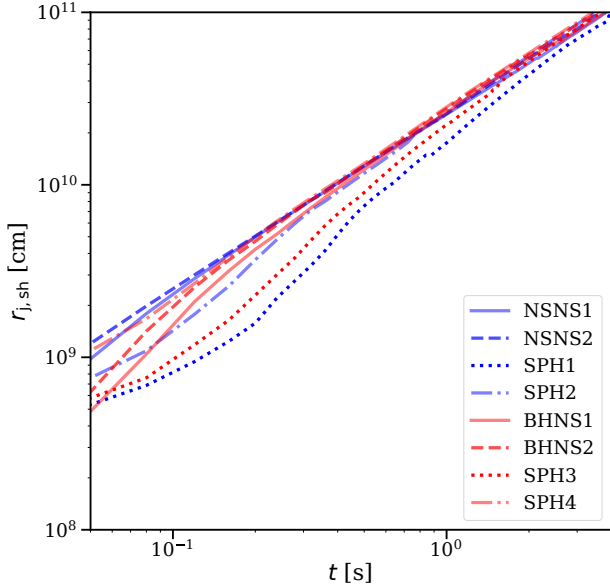


**Figure 7.** The evolution of the shock front position of the jet, presented in logarithmic scale. The jet models associated with the NSNS merger scenario are denoted with blue, while the red colour denotes the BHNS merger scenario. For both scenarios, the continuous lines describe jets with interaction of dynamical ejecta at the first fraction of a second. Dashed lines describe the jet propagation without initial ejecta. Dotted lines represent the jets with  $\theta_j = 15^\circ$  and whose propagation is into a spherical atmosphere without disk wind injection. The dotted-dashed line describes the jet propagation in SPH atmosphere but more collimated  $\theta_j = 1/\Gamma_j$ . The plots show that a jet implemented with  $\theta_j > 1/\Gamma_j$  is collimated by the wind in the NSNS scenario, while BHNS scenario presents the opposite result.

drilling efficiently into the atmosphere, and resulting in a substantial accumulation of mass ahead of the jet.

Fig. 8 shows the energy structure of the jet, cocoon, and wind, determined by eqs. (12), (13), and (15), respectively. In panel a), we observe a similar structure for both jets NSNS1 and NSNS2 with only minor variations in the collimation between them. A similar effect is observed in panel d) for models BHNS1 and BHNS2, except for the asymmetry located at the south pole in model BHNS2 where the jet exhibits a notable extension of 10 degrees, larger compared to model BHNS1.

More significant differences and asymmetries can be observed in the energy distribution of the cocoon, in panels b) and e). Panel b) shows that the PME have different impact on the cocoon expansion in NSNS mergers, because in this scenario, the jets maintain a higher degree of collimation. In the BHNS2 model, apparently the cocoon expansion is influenced by the initial PME and a poorly collimated jet, as illustrated in panel e).

The energy distribution of the wind in the models presented in panels c) and f) exhibits minimal discrepancies

between the scenarios with and without PME. A distinctive contrast emerges when comparing the NSNS and BHNS scenarios, particularly in the equatorial region.

Panel g) provides a global illustration and shows all three energy components. Additionally, this panel provides a comparison between the two scenarios.

Panels h) and i) show the impact of the disk wind on the evolution of the jet and cocoon. To examine this effect, models NSNS2 and BHNS2 are compared to jet models injected into a spherical PME (SPH1-SPH4). From panel h), it is evident that the NSNS2 jet is collimated with a cocoon exhibiting less lateral spreading compared to the manually collimated jet SPH2 and the initially non-collimated jet SPH1. Therefore, it is observed that the disk wind induces collimation and blocks the lateral spreading of the cocoon.

On the other hand, in panel i), the BHNS2 jet presents a similar lateral spreading as in the non-collimated jet SPH3, while it exceeds the lateral spreading of the collimated case SPH4. In this scenario, the disk wind presents a different sideways expansion and the jet collimation is less efficient with respect to the model NSNS2.

In Fig. 9 we present the time evolution of the kinetic and thermal energy, separately for the jet, cocoon, and wind, in the models with PME ejecta. In the following paragraphs, we describe the evolution of each component.

The jet evolution proceeds as follows. At the beginning, the thermal energy dominates over the kinetic because the jet injection is pressure dominated. At late times, kinetic and thermal energies have the same order of magnitude. The jet region does not present a complete conversion of the thermal to kinetic energy.

The cocoon evolution is the following. The final shape (at late times) results from the continuous interaction with the jet, where the energy injection takes place close to the poles. In the case of NSNS2 model, which presents a more collimated jet, the kinetic energy dominates over the thermal energy at late times, across the jet, because thermal energy is converted into kinetic energy. The model BHNS2 presents a similar distribution of thermal and kinetic energy, albeit there is a slower transfer of thermal energy to kinetic.

In the polar region, the kinetic energy of the wind is more dominant than its thermal energy. This area contains the most external material within the system, interacting with a simple external medium. As a result, this material is freely expanding. On the other hand, at the equator, both kinetic and thermal components contribute equally, as materials from both poles collide, form shocks and provide subsequent heating. Here, the

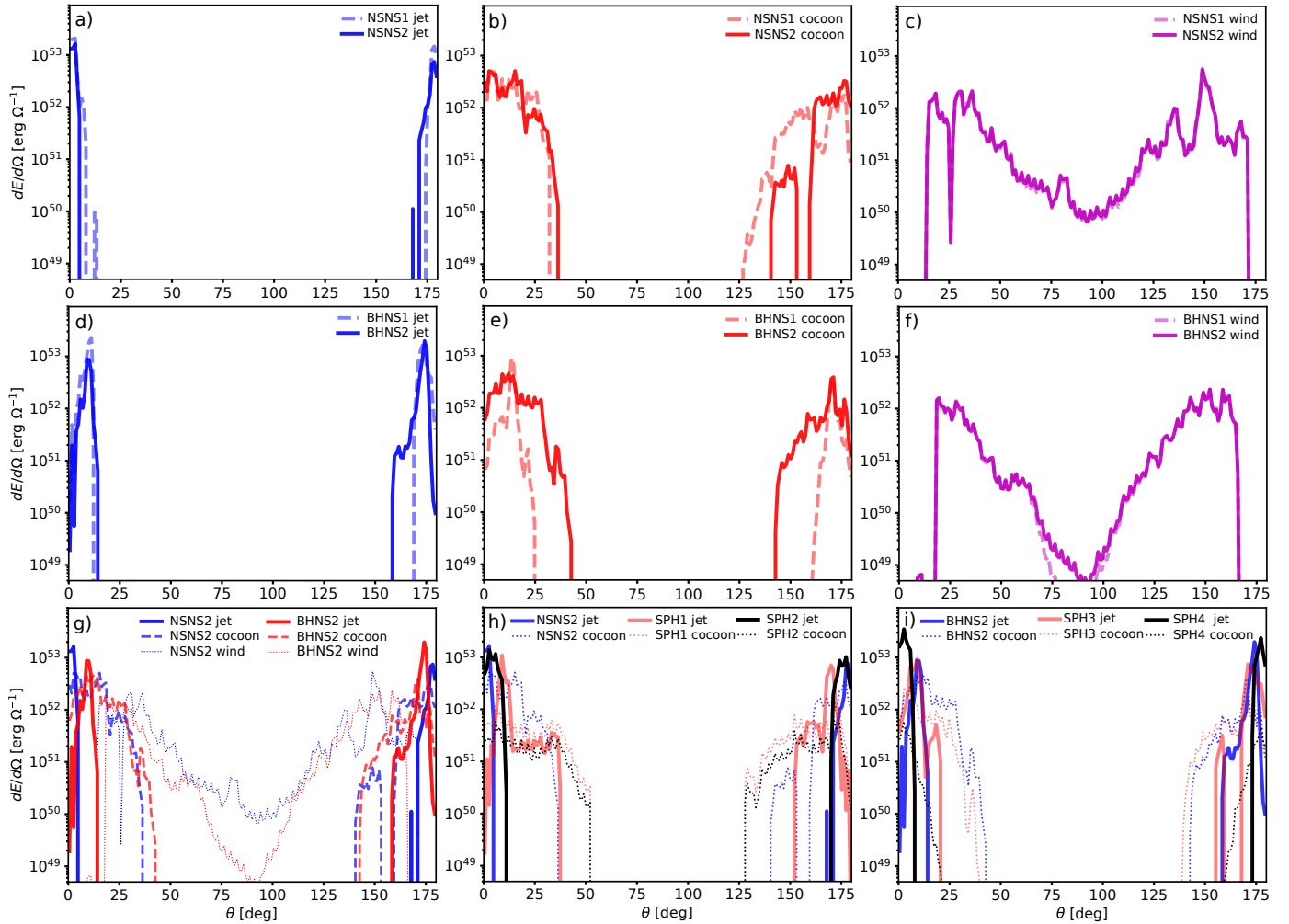


**Figure 8.** The energy distribution at  $t = 2$  s, estimated by eqs. (11)-(15). The energy within the jet is determined by the contribution from fluid exhibiting high Lorentz factors  $\Gamma \geq \Gamma_j$ . In contrast, the energy content of the cocoon derives from material moving within a range where  $\Gamma_j > \Gamma \geq 2$ . Finally, the slower material contributes to the energy of the wind. In panels a) through c), we illustrate each of these energy contributions and a comparison between two distinct models for NSNS scenario. A similar comparison is provided in panels d) through f) for the BHNS scenario. Panel g) shows a comparison between the NSNS2 and BHNS2 models. Panels h) and i) present the comparisons related to jet collimation and cocoon expansion.

kinetic contribution is low due to the slower velocities of the wind in this region.

#### 4. DISCUSSION

The interaction between short GRB jets and their expanding post-merger environment significantly modifies the propagation and structure of these jets (e.g., Salafia & Ghirlanda 2022, and references therein). Our results emphasize the critical need for the distinction of the components within the post-merger environments (Fig. 1). Each component provides a unique influence on the propagation and structure of the jet. Specifically, in this study, we focused on exploring the impact of the post-merger disk wind on the dynamics of short GRB jets at larger scales. The disk wind employed in our simulations resulted from the interplay of magnetized

wind dynamics and neutrino cooling. Then, this element presents a more realistic scenario compared to the standard homogeneously expanding wind. Moreover, our numerical setup considers the contribution of r-process nucleosynthesis and its effect on gas pressure.

##### 4.1. The influence of the disk-wind outflow in the jet propagation

Our results highlight the primary elements influencing the jet propagation: 1) density in front of the jet head, 2) pressure exerted by the post-merger environment, and 3) turbulence in the transition region between the jet and the environment.

A realistic density distribution of post-merger winds exhibits an expanded toroidal pattern, with a low-density region in the jet funnel. For example, our models

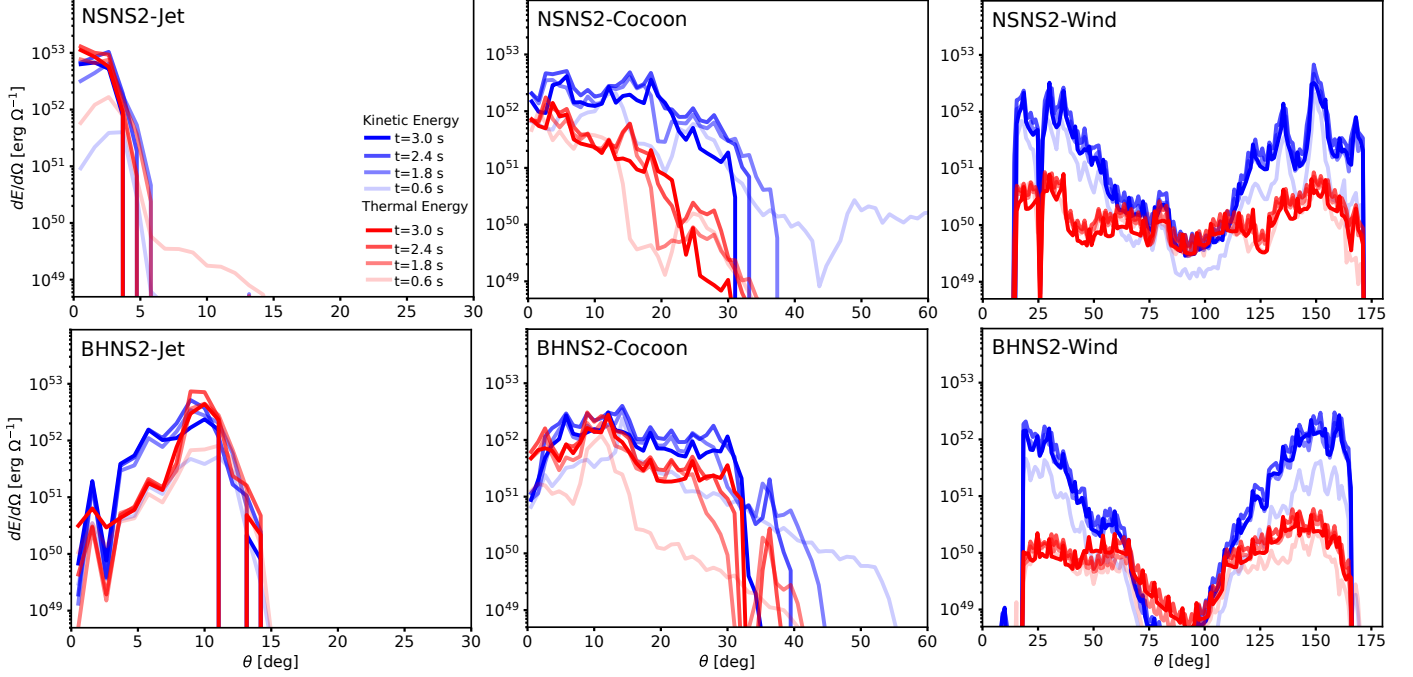


**Figure 9.** The energy evolution of each contribution for both the NSNS2 model (upper panel) and the BHNS2 model (lower panel). In this plot, thermal energy is represented by the colour red, while kinetic energy is depicted in blue, following the definitions as outlined in eqs (5), (6), and (11)-(15).

(see Fig. 3) show a lighter material concentrated near to the jet funnel and heavier material accumulating in the equatorial regions. In this scenario, the shock front of the jet carries less dense material (e.g., Aloy et al. 2005; Murguia-Berthier et al. 2017), contrasted with the case of the spherical distribution (See Fig. 7). Additionally, the propagation of the jet is influenced by the initial opening angle  $\theta_j$ , which indicates that the jet is collimated if the criteria  $\theta_j < \Gamma_j^{-1}$  is satisfied (Bromberg et al. 2011). A bow shock is pronounced for non collimated jets making suitable the accumulation of the material in front of the jet (e.g., Aloy et al. 2005; Hamidani et al. 2020; Nativi et al. 2020; Urrutia et al. 2021; Gottlieb & Nakar 2021). In our study, non-collimated SPH models produce slower expansion compared to collimated ones. Notably, jets propagating in distributed winds (such as NSNS and BHNS) initially manifest as non-collimated, however, their fast expansion is not impeded.

The collimation of the jet ( $\theta_j < \Gamma_j^{-1}$ ) has been studied through the balance of pressures between the jet and a uniform environment (Bromberg et al. 2011), and the jet remains collimated by the condition

$$\rho_j h_j \Gamma_j^2 / \rho_w < \theta_j^{-4/3}. \quad (17)$$

Notwithstanding, this criterion was developed for uniform environments. Examining different jet opening angles in combination with post-merger environment sce-

narios reveals the influence of the realistic post-merger wind in the jet collimation. Specifically, is observed in models transitioning from non-collimated to collimated states, such as NSNS1 and NSNS2. However, generalizing these findings based on assumptions about source properties may not hold universally, such is the case of BHNS1 and BHNS2, where the jet remains uncollimated.

The expansion of the cocoon is also modified by the interaction with post-merger disk wind and the post-merger ejecta (Fig. 8). The pressure and velocity distribution of the wind either expand or compress the cocoon material. Moreover, our realistic models (eg., NSNS2 and BHNS2) exhibiting higher turbulence undergo more substantial modifications.

The turbulence mainly arises from two mechanisms. Firstly, Kelvin-Helmholtz instabilities are generated as a result of shearing layers interacting with different velocities, in particular, the high-speed velocity of the jet and the slower disk wind in the region of interaction (e.g., Perucho, M. et al. 2004). Secondly, turbulence is induced by the diffusion of both the jet and the wind, occurring in the transition region between PME (EJ) and the constant external medium  $\rho_a$  (the breakout region transition). In addition, the propagation of relativistic jets can produce oscillation induced Raleigh-Taylor instabilities (e.g., Matsumoto & Masada 2019), however it is not clear whether their onset conditions would be

satisfied in our jet-cocoon system, and they are hard to probe in the axisymmetric setup.

To demonstrate an increase in turbulence induced by the presence of the disk wind in our models, compared to the homologous case, we estimate the growth of instabilities at an arbitrarily chosen reference point with turbulence  $(x_{\text{ref}}, z_{\text{ref}}) = (0.08, 0.14) c$ . At this point, we apply growth estimation described in (e.g., Kifonidis, K. et al. 2003; Iwamoto et al. 1997; Mueller et al. 1991), it is estimated as

$$\sigma = \sqrt{-\frac{p}{\rho} \frac{\partial \ln p}{\partial r} \frac{\partial \ln \rho}{\partial r}}. \quad (18)$$

The relative pressure and density gradient quantify the amount of instabilities ones the relative point is reached by the launched material. The value time evolution of  $\sigma$  is measured when the launched material crosses the reference point (Fig 10).

#### 4.2. The effects of the central engine in the jet structure

The development of a structured jet is evident from the angular distribution observed in the Lorentz factor and luminosity during the propagation at small scales (Kathirgamaraju et al. 2019; James et al. 2022; Janiuk & James 2022). Here, the turbulence in the central engine can have some effect on the temporal variability of the emitted jet and this can in turn be propagated to larger scales. This turbulence can be driven by various instabilities in the plasma inflow in the disk including magnetorotational instability (MRI) in the case of weakly magnetized disks or through magnetic reconnections and interchange instability in the case of magnetically arrested accretion disks (MAD).

In addition, the post-merger environment potentially affects the jet structure due to the collimation criteria (Eq. 17). In terms of the mass loss rate, it can be written as  $\dot{M}_w < 2L_j v_w / r_j^2 \theta_j^{2/3}$ , to set the limit on this value (e.g., Urrutia et al. 2022), i.e.,  $\dot{M}_w < 1.5 \times 10^{-3} \left( \frac{L_j}{10^{51} \text{ ergs s}^{-1}} \right) \left( \frac{\theta_j}{0.1} \right)^{-2/3} \left( \frac{r_j}{10^9 \text{ cm}} \right)^{-2} \left( \frac{v_w}{0.3c} \right)$ . Below this limit, the jet can expand laterally and its structure from the central engine is partially preserved (e.g., Urrutia et al. 2021), and the structure is reshaped for dense environments (Nativi et al. 2022; Urrutia et al. 2022). Therefore, in our implementation, neither a structured jet at the launch point nor the central engine variability have been included due to our environment's characteristics, although further studies could validate these conditions.

#### 4.3. The evolution of energy distributions and implications to large scales

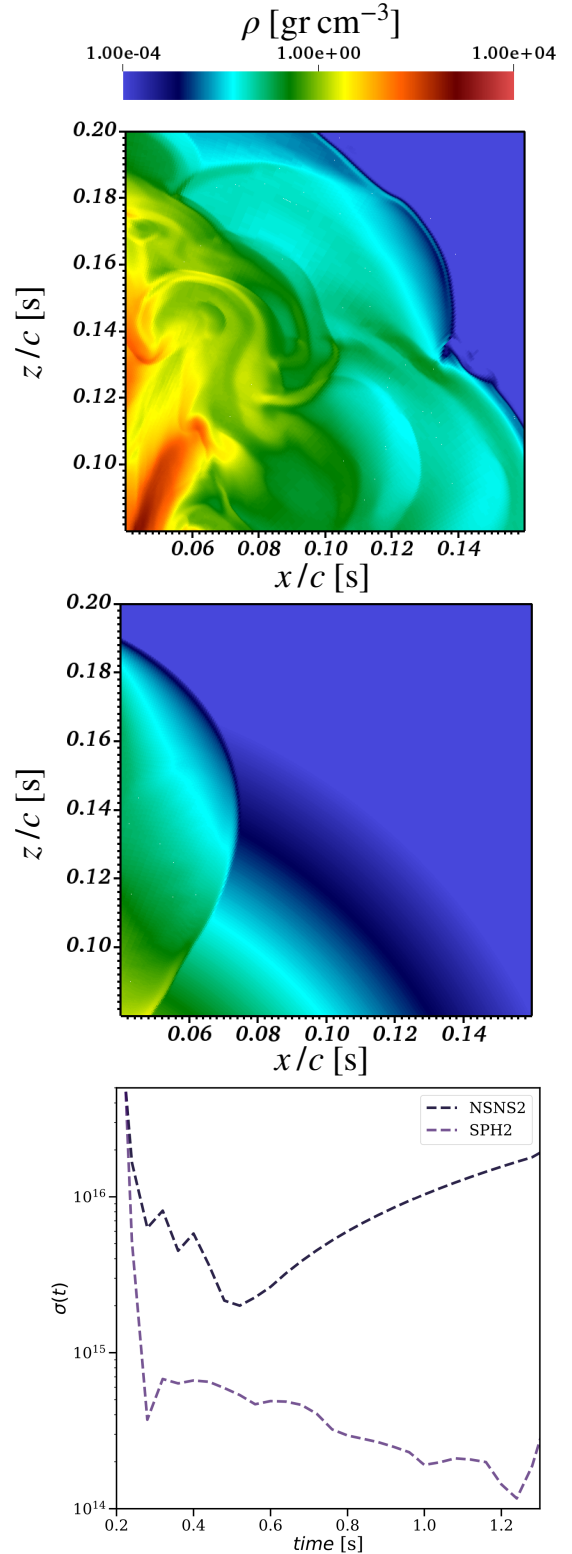


**Figure 10.** Upper and central panels: density map comparison between models NSNS2 and SPH2 at  $t = 0.2$  s. Bottom panel: temporal growth of instabilities at  $(0.08, 0.14) c$  estimated from Eq. (18).

Throughout our simulations, the dominance of thermal energy within the jet persists to late times, indicating that interactions with the cocoon are primarily driven by thermal energy transfer. The energy evolution of the cocoon is notably shaped by the components of the post-merger environment. For example, in the model NSNS2 (Fig. 9), the interaction between the cocoon and disk-wind is dominated by the kinetic energy, which suggests this region is shaped by the velocity distribution. On the other hand, the model BHNS2 exhibits a thermalized cocoon at late times.

Homologous expansion, achieved only through complete thermal-to-kinetic energy conversion, occurs distinctly in the system. While the distribution of heavy wind material, especially close to the polar regions, experiences dominant kinetic energy expansion, this expansion is non-uniform. The simple scenario assumes a homologous wind expansion, yet significant thermal energy retention occurs in the polar regions. Disruptions in the jet’s kinetic energy conversion by the high-speed material in the equatorial regions may impact estimations of the jet emission, warranting careful modeling in the future kilonova studies.

In previous studies (e.g., Aloy et al. 2005; Duffell et al. 2015, 2018; Hamidani et al. 2020; Urrutia et al. 2021; Murguia-Berthier et al. 2021; Hamidani & Ioka 2023), the long evolution of the cocoon results in an expansion to engulf the post-merger wind. This effect occurs because the velocity of the cocoon exceeds the uniform velocity of the homologous wind. However, in our scenarios, the initial wind material presents higher velocities close to the jet region (Fig. 3). Consequently, this faster wind material moves together with the cocoon, and even in some cases it becomes polluted. In the unique case of BHNS2, the cocoon engulfs the post-merger wind (Fig 6).

An important application of the jet and cocoon evolution at large scales involves extrapolating energy distributions to distances of  $r \sim 10^{16}$  cm, to estimate the afterglow radiation (e.g., Duffell et al. 2018; Lazduti et al. 2018; Mooley et al. 2018; Nathanail et al. 2020; Urrutia et al. 2021; Dichiaro et al. 2021; Nativi et al. 2022; Mpisketzis et al. 2024). Our results suggest the necessity of modifying energy distribution at these large scales, where the transformation from thermal to kinetic energy becomes significant. However, this transition would be more comprehensively studied through the evolution over larger distances (at least  $r \gtrsim 10^{13}$  cm). It is a potential application of our models for the future observations of *off-axis* GRB and the upcoming multi-wavelength surveys (e.g., Salafia et al. 2016; Ghirlanda et al. 2019; Gottlieb et al. 2019; Dichiaro et al. 2021)

## 5. CONCLUSIONS

We perform two-dimensional SRHD numerical simulations to study the large-scale interaction between short GRB jets with the post-merger disk wind outflows. These winds were remapped from the previous GRMHD simulations of post-merger black hole accretion disk evolution. In particular, we follow the evolution of jets and outflows arising from NSNS and BHNS scenarios.

Our results show crucial differences when compared to common models using homologous expanding winds:

- Since we considered the impact of the nuclear heating via r-process on the initial wind pressure, we observed that it leads to significant alterations in both jet collimation and cocoon expansion rate.
- Density and velocity distribution of the wind induces a turbulent environment and provides asymmetric jets.
- The angular structure of the energy components (thermal and kinetic) for the jet, cocoon, and wind present crucial differences with respect to homologous models. This implies that the GRB afterglow emission for the *off-axis* observers will be modified, since the radiation estimation is strongly connected with the energy distribution.
- During the time evolution of the jet thermal energy is not converted into kinetic. The cocoon in the model NSNS2 presents conversion of thermal energy at large angles and is preserved in the same order of magnitude as for the model BHNS2. The kinetic energy of the wind dominates close to the poles and thermal energy dominates at the equator.

Notwithstanding, the energy structure and the expansion of the expelled material is a consequence of the assumed configuration, namely wither NSNS or BHNS merger. The results are sensitive to the interaction of the jet and the disk wind with the post-merger environment. It is shown, for example, by tracking the evolution of chemical composition of the disk-wind outflow.

- The post-merger environment induces turbulence, leading to the material disperse more widely and limiting free expansion. As a result, the interaction between the jet and the disk wind becomes more pronounced.
- In the post-merger scenario of NSNS, the poor lanthanide material (more opaque) tends to accumulate near the equator, while the more transparent

material is found closer to the poles. However, in the case of BHNS, the distribution remains more mixed

- The jet remains free of pollution.

For this study, we did not consider the influence of magnetic fields on the large-scale evolution. The presence of magnetic fields is crucial to get more collimated and stable jets, particularly when they are polluted by the progenitor environment (e.g., [Gottlieb & Nakar 2021](#); [García-García et al. 2023](#); [Pavan et al. 2023](#)). However, our jet models did not acquire pollution.

Our study emphasizes the critical influence of the post-merger disk wind on jet propagation. This element needs to be managed meticulously because the main characteristics are susceptible to the engine characteristics, such as spin, magnetic field strength, and neutrino cooling. This means that is important to select

the parameters that distinguish each scenario to avoid future degeneracy in the interpretation of electromagnetic counterparts.

Finally, despite our disk wind being more realistic than homologous cases, the post-merger ejecta (expelled during the merger) employed for the models NSNS2 and BHNS2 are a simplified version of a realistic case. The results would be improved if the realistic disk-wind models were embedded in post-merger environments.

- 1 This work was supported by the grant
- 2 2019/35/B/ST9/04000 from Polish National Science
- 3 Center. This research was also supported by PLGrid
- 4 Infrastructure under grant plggrb6, and Warsaw ICM.
- 5 We thank to Fabio De Colle, Diego Lopez-Camara,
- 6 Leonardo Garcia-Garcia and Enrique Moreno for useful
- 7 discussions.

## REFERENCES

- Abbott, B. P., Abbott, R., Abbott, T. D., et al. 2017, *Phys. Rev. Lett.*, 119, 161101, doi: [10.1103/PhysRevLett.119.161101](https://doi.org/10.1103/PhysRevLett.119.161101)
- Aloy, M. A., Janka, H.-T., & Müller, E. 2005, *A&A*, 436, 273, doi: [10.1051/0004-6361:20041865](https://doi.org/10.1051/0004-6361:20041865)
- Balbus, S. A., & Hawley, J. F. 2002, *ApJ*, 573, 749, doi: [10.1086/340767](https://doi.org/10.1086/340767)
- Beniamini, P., Duran, R. B., Petropoulou, M., & Giannios, D. 2020, *ApJL*, 895, L33, doi: [10.3847/2041-8213/ab9223](https://doi.org/10.3847/2041-8213/ab9223)
- Berger, E. 2011, *NewAR*, 55, 1, doi: [10.1016/j.newar.2010.10.001](https://doi.org/10.1016/j.newar.2010.10.001)
- Blandford, R. D., & Znajek, R. L. 1977, *MNRAS*, 179, 433, doi: [10.1093/mnras/179.3.433](https://doi.org/10.1093/mnras/179.3.433)
- Bromberg, O., Nakar, E., Piran, T., & Sari, R. 2011, *APJ*, 740, 100, doi: [10.1088/0004-637X/740/2/100](https://doi.org/10.1088/0004-637X/740/2/100)
- Ciolfi, R., Kastaun, W., Giacomazzo, B., et al. 2017, *PhRvD*, 95, 063016, doi: [10.1103/PhysRevD.95.063016](https://doi.org/10.1103/PhysRevD.95.063016)
- Ciolfi, R., Kastaun, W., Kalinani, J. V., & Giacomazzo, B. 2019, *Phys. Rev. D*, 100, 023005, doi: [10.1103/PhysRevD.100.023005](https://doi.org/10.1103/PhysRevD.100.023005)
- Combi, L., & Siegel, D. M. 2023, *Jets from neutron-star merger remnants and massive blue kilonovae*. <https://arxiv.org/abs/2303.12284>
- De Colle, F., Granot, J., López-Cámara, D., & Ramirez-Ruiz, E. 2012, *ApJ*, 746, 122, doi: [10.1088/0004-637X/746/2/122](https://doi.org/10.1088/0004-637X/746/2/122)
- Dichiara, S., Becerra, R. L., Chase, E. A., et al. 2021, *The Astrophysical Journal Letters*, 923, L32, doi: [10.3847/2041-8213/ac4259](https://doi.org/10.3847/2041-8213/ac4259)
- Duffell, P. C., Quataert, E., Kasen, D., & Klion, H. 2018, *APJ*, 866, 3, doi: [10.3847/1538-4357/aae084](https://doi.org/10.3847/1538-4357/aae084)
- Duffell, P. C., Quataert, E., & MacFadyen, A. I. 2015, *APJ*, 813, 64, doi: [10.1088/0004-637X/813/1/64](https://doi.org/10.1088/0004-637X/813/1/64)
- Eichler, D., Livio, M., Piran, T., & Schramm, D. N. 1989, *Nature*, 340, 126, doi: [10.1038/340126a0](https://doi.org/10.1038/340126a0)
- Fahlman, S., & Fernández, R. 2022, *MNRAS*, doi: [10.1093/mnras/stac948](https://doi.org/10.1093/mnras/stac948)
- Fernández, R., Tchekhovskoy, A., Quataert, E., Foucart, F., & Kasen, D. 2019, *MNRAS*, 482, 3373, doi: [10.1093/mnras/sty2932](https://doi.org/10.1093/mnras/sty2932)
- Foucart, F., Deaton, M. B., Duez, M. D., et al. 2013, *PhRvD*, 87, 084006, doi: [10.1103/PhysRevD.87.084006](https://doi.org/10.1103/PhysRevD.87.084006)
- Gammie, C. F., McKinney, J. C., & Tóth, G. 2003, *The Astrophysical Journal*, 589, 444, doi: [10.1086/374594](https://doi.org/10.1086/374594)
- García-García, L., López-Cámara, D., & Lazzati, D. 2023, *Monthly Notices of the Royal Astronomical Society*, 519, 4454, doi: [10.1093/mnras/stad023](https://doi.org/10.1093/mnras/stad023)
- Ghirlanda, G., Salafia, O. S., Paragi, Z., et al. 2019, *Science*, 363, 968, doi: [10.1126/science.aau8815](https://doi.org/10.1126/science.aau8815)
- Gill, R., Granot, J., De Colle, F., & Urrutia, G. 2019, *APJ*, 883, 15, doi: [10.3847/1538-4357/ab3577](https://doi.org/10.3847/1538-4357/ab3577)
- Gottlieb, O., Moseley, S., Ramirez-Aguilar, T., et al. 2022, *The Astrophysical Journal Letters*, 933, L2, doi: [10.3847/2041-8213/ac7728](https://doi.org/10.3847/2041-8213/ac7728)
- Gottlieb, O., & Nakar, E. 2021, *arXiv e-prints*, arXiv:2106.03860. <https://arxiv.org/abs/2106.03860>



- Gottlieb, O., Nakar, E., & Piran, T. 2019, *Monthly Notices of the Royal Astronomical Society*, 488, 2405, doi: [10.1093/mnras/stz1906](https://doi.org/10.1093/mnras/stz1906)
- Gottlieb, O., Issa, D., Jacquemin-Ide, J., et al. 2023, *The Astrophysical Journal Letters*, 954, L21, doi: [10.3847/2041-8213/aceeff](https://doi.org/10.3847/2041-8213/aceeff)
- Granot, J., Gill, R., Guetta, D., & De Colle, F. 2018, *MNRAS*, 481, 1597, doi: [10.1093/mnras/sty2308](https://doi.org/10.1093/mnras/sty2308)
- Grossman, D., Korobkin, O., Rosswog, S., & Piran, T. 2014, *MNRAS*, 439, 757, doi: [10.1093/mnras/stt2503](https://doi.org/10.1093/mnras/stt2503)
- Guilet, J., Bauswein, A., Just, O., & Janka, H.-T. 2017, *MNRAS*, 471, 1879, doi: [10.1093/mnras/stx1739](https://doi.org/10.1093/mnras/stx1739)
- Guilet, J., Müller, E., & Janka, H.-T. 2015, *MNRAS*, 447, 3992, doi: [10.1093/mnras/stu2550](https://doi.org/10.1093/mnras/stu2550)
- Hamidani, H., & Ioka, K. 2023, *MNRAS*, 524, 4841, doi: [10.1093/mnras/stad1933](https://doi.org/10.1093/mnras/stad1933)
- Hamidani, H., Kiuchi, K., & Ioka, K. 2020, *MNRAS*, 491, 3192, doi: [10.1093/mnras/stz3231](https://doi.org/10.1093/mnras/stz3231)
- Hossein Nouri, F., Duez, M. D., Foucart, F., et al. 2018, *Phys. Rev. D*, 97, 083014, doi: [10.1103/PhysRevD.97.083014](https://doi.org/10.1103/PhysRevD.97.083014)
- Iwamoto, K., Young, T. R., Nakasato, N., et al. 1997, *ApJ*, 477, 865, doi: [10.1086/303729](https://doi.org/10.1086/303729)
- James, B., Janiuk, A., & Nouri, F. H. 2022, *The Astrophysical Journal*, 935, 176, doi: [10.3847/1538-4357/ac81b7](https://doi.org/10.3847/1538-4357/ac81b7)
- Janiuk, A. 2017, *ApJ*, 837, 39, doi: [10.3847/1538-4357/aa5f16](https://doi.org/10.3847/1538-4357/aa5f16)
- . 2019, *ApJ*, 882, 163, doi: [10.3847/1538-4357/ab3349](https://doi.org/10.3847/1538-4357/ab3349)
- Janiuk, A., & James, B. 2022, *A&A*, 668, A66, doi: [10.1051/0004-6361/202244196](https://doi.org/10.1051/0004-6361/202244196)
- Janiuk, A., Mioduszewski, P., & Moscibrodzka, M. 2013, *ApJ*, 776, 105, doi: [10.1088/0004-637X/776/2/105](https://doi.org/10.1088/0004-637X/776/2/105)
- Janiuk, A., & Proga, D. 2008, *ApJ*, 675, 519, doi: [10.1086/526511](https://doi.org/10.1086/526511)
- Kasen, D., Fernández, R., & Metzger, B. D. 2015, *MNRAS*, 450, 1777, doi: [10.1093/mnras/stv721](https://doi.org/10.1093/mnras/stv721)
- Kasen, D., Metzger, B., Barnes, J., Quataert, E., & Ramirez-Ruiz, E. 2017, *Nature*, 551, 80, doi: [10.1038/nature24453](https://doi.org/10.1038/nature24453)
- Kathirgamaraju, A., Tchekhovskoy, A., Giannios, D., & Barniol Duran, R. 2019, *MNRAS*, 484, L98, doi: [10.1093/mnrasl/slz012](https://doi.org/10.1093/mnrasl/slz012)
- Kawaguchi, K., Kyutoku, K., Shibata, M., & Tanaka, M. 2016, *The Astrophysical Journal*, 825, 52, doi: [10.3847/0004-637x/825/1/52](https://doi.org/10.3847/0004-637x/825/1/52)
- Kifonidis, K., Plewa, T., Janka, H.-Th., & Müller, E. 2003, *A&A*, 408, 621, doi: [10.1051/0004-6361:20030863](https://doi.org/10.1051/0004-6361:20030863)
- Kluźniak, W., & Lee, W. H. 1998, *ApJL*, 494, L53, doi: [10.1086/311151](https://doi.org/10.1086/311151)
- Krüger, C. J., & Foucart, F. 2020, *Phys. Rev. D*, 101, 103002, doi: [10.1103/PhysRevD.101.103002](https://doi.org/10.1103/PhysRevD.101.103002)
- Lazzati, D., Perna, R., Ciolfi, R., et al. 2021, *The Astrophysical Journal Letters*, 918, L6, doi: [10.3847/2041-8213/ac1794](https://doi.org/10.3847/2041-8213/ac1794)
- Lazzati, D., Perna, R., Morsony, B. J., et al. 2018, *PRL*, 120, 241103, doi: [10.1103/PhysRevLett.120.241103](https://doi.org/10.1103/PhysRevLett.120.241103)
- Lee, W. H., & Ramirez-Ruiz, E. 2002, *ApJ*, 577, 893, doi: [10.1086/342112](https://doi.org/10.1086/342112)
- Lippuner, J., & Roberts, L. F. 2017, *The Astrophysical Journal Supplement Series*, 233, 18, doi: [10.3847/1538-4365/aa94cb](https://doi.org/10.3847/1538-4365/aa94cb)
- Liu, T., Lin, Y.-Q., Hou, S.-J., & Gu, W.-M. 2015, *ApJ*, 806, 58, doi: [10.1088/0004-637X/806/1/58](https://doi.org/10.1088/0004-637X/806/1/58)
- Lovelace, G., Duez, M. D., Foucart, F., et al. 2013, *Classical and Quantum Gravity*, 30, 135004, doi: [10.1088/0264-9381/30/13/135004](https://doi.org/10.1088/0264-9381/30/13/135004)
- Martin, D., Perego, A., Arcones, A., et al. 2015, *ApJ*, 813, 2, doi: [10.1088/0004-637X/813/1/2](https://doi.org/10.1088/0004-637X/813/1/2)
- Matsumoto, J., & Masada, Y. 2019, *MNRAS*, 490, 4271, doi: [10.1093/mnras/stz2821](https://doi.org/10.1093/mnras/stz2821)
- Metzger, B. D., & Berger, E. 2012, *The Astrophysical Journal*, 746, 48, doi: [10.1088/0004-637X/746/1/48](https://doi.org/10.1088/0004-637X/746/1/48)
- Metzger, B. D., Martínez-Pinedo, G., Darbha, S., et al. 2010, *MNRAS*, 406, 2650, doi: [10.1111/j.1365-2966.2010.16864.x](https://doi.org/10.1111/j.1365-2966.2010.16864.x)
- Mignone, A., & Bodo, G. 2005, *Monthly Notices of the Royal Astronomical Society*, 364, 126, doi: [10.1111/j.1365-2966.2005.09546.x](https://doi.org/10.1111/j.1365-2966.2005.09546.x)
- Mooley, K. P., Deller, A. T., Gottlieb, O., et al. 2018, *Nature*, 561, 355, doi: [10.1038/s41586-018-0486-3](https://doi.org/10.1038/s41586-018-0486-3)
- Mpisketzis, V., Duqué, R., Nathanail, A., Cruz-Orsorio, A., & Rezzolla, L. 2024, *MNRAS*, 527, 9159, doi: [10.1093/mnras/stad3774](https://doi.org/10.1093/mnras/stad3774)
- Mueller, E., Fryxell, B., & Arnett, D. 1991, *A&A*, 251, 505
- Murguia-Berthier, A., Montes, G., Ramirez-Ruiz, E., De Colle, F., & Lee, W. H. 2014, *ApJL*, 788, L8, doi: [10.1088/2041-8205/788/1/L8](https://doi.org/10.1088/2041-8205/788/1/L8)
- Murguia-Berthier, A., Ramirez-Ruiz, E., Colle, F. D., et al. 2021, *The Astrophysical Journal*, 908, 152, doi: [10.3847/1538-4357/abd08e](https://doi.org/10.3847/1538-4357/abd08e)
- Murguia-Berthier, A., Ramirez-Ruiz, E., Montes, G., et al. 2017, *ApJL*, 835, L34, doi: [10.3847/2041-8213/aa5b9e](https://doi.org/10.3847/2041-8213/aa5b9e)
- Murguia-Berthier, A., Ramirez-Ruiz, E., Kilpatrick, C. D., et al. 2017, *The Astrophysical Journal Letters*, 848, L34, doi: [10.3847/2041-8213/aa91b3](https://doi.org/10.3847/2041-8213/aa91b3)
- Murguia-Berthier, A., Ramirez-Ruiz, E., Montes, G., et al. 2017, *ApJL*, 835, L34, doi: [10.3847/2041-8213/aa5b9e](https://doi.org/10.3847/2041-8213/aa5b9e)

- Nathanail, A., Gill, R., Porth, O., Fromm, C. M., & Rezzolla, L. 2020, arXiv e-prints, arXiv:2009.09714. <https://arxiv.org/abs/2009.09714>
- Nativi, L., Bulla, M., Rosswog, S., et al. 2020, *Monthly Notices of the Royal Astronomical Society*, 500, 1772, doi: [10.1093/mnras/staa3337](https://doi.org/10.1093/mnras/staa3337)
- Nativi, L., Lamb, G. P., Rosswog, S., Lundman, C., & Kowal, G. 2022, *MNRAS*, 509, 903, doi: [10.1093/mnras/stab2982](https://doi.org/10.1093/mnras/stab2982)
- Nouri, F. H., Janiuk, A., & Przerwa, M. 2023, *The Astrophysical Journal*, 944, 220, doi: [10.3847/1538-4357/acafe2](https://doi.org/10.3847/1538-4357/acafe2)
- Paczynski, B. 1991, *AcA*, 41, 257
- Pavan, A., Ciolfi, R., Kalinani, J. V., & Mignone, A. 2021, *Monthly Notices of the Royal Astronomical Society*, 506, 3483, doi: [10.1093/mnras/stab1810](https://doi.org/10.1093/mnras/stab1810)
- . 2023, *Monthly Notices of the Royal Astronomical Society*, 524, 260, doi: [10.1093/mnras/stad1809](https://doi.org/10.1093/mnras/stad1809)
- Perego, A., Rosswog, S., Cabezón, R. M., et al. 2014, *MNRAS*, 443, 3134, doi: [10.1093/mnras/stu1352](https://doi.org/10.1093/mnras/stu1352)
- Perucho, M., Hanasz, M., Martí, J. M., & Sol, H. 2004, *A&A*, 427, 415, doi: [10.1051/0004-6361:20040349](https://doi.org/10.1051/0004-6361:20040349)
- Popham, R., Woosley, S. E., & Fryer, C. 1999, *ApJ*, 518, 356, doi: [10.1086/307259](https://doi.org/10.1086/307259)
- Rosswog, S., & Korobkin, O. 2022, *Annalen der Physik*, 2200306, doi: <https://doi.org/10.1002/andp.202200306>
- Salafia, O. S., & Ghirlanda, G. 2022, *Galaxies*, 10, doi: [10.3390/galaxies10050093](https://doi.org/10.3390/galaxies10050093)
- Salafia, O. S., Ghisellini, G., Pescalli, A., Ghirlanda, G., & Nappo, F. 2016, *MNRAS*, 461, 3607, doi: [10.1093/mnras/stw1549](https://doi.org/10.1093/mnras/stw1549)
- Sano, T., Inutsuka, S.-i., Turner, N. J., & Stone, J. M. 2004, *ApJ*, 605, 321, doi: [10.1086/382184](https://doi.org/10.1086/382184)
- Suzuki, A., & Maeda, K. 2022, *ApJ*, 925, 148, doi: [10.3847/1538-4357/ac3d8d](https://doi.org/10.3847/1538-4357/ac3d8d)
- Tanaka, M., Utsumi, Y., Mazzali, P. A., et al. 2017, *PASJ*, 69, 102, doi: [10.1093/pasj/psx121](https://doi.org/10.1093/pasj/psx121)
- Timmes, F. X., & Arnett, D. 1999, *ApJS*, 125, 277, doi: [10.1086/313271](https://doi.org/10.1086/313271)
- Urrutia, G., De Colle, F., & López-Cámara, D. 2022, *Monthly Notices of the Royal Astronomical Society*, 518, 5145, doi: [10.1093/mnras/stac3401](https://doi.org/10.1093/mnras/stac3401)
- Urrutia, G., De Colle, F., Murguía-Berthier, A., & Ramírez-Ruiz, E. 2021, *Monthly Notices of the Royal Astronomical Society*, 503, 4363, doi: [10.1093/mnras/stab723](https://doi.org/10.1093/mnras/stab723)
- Woosley, S. E., & Hoffman, R. D. 1992, *ApJ*, 395, 202, doi: [10.1086/171644](https://doi.org/10.1086/171644)